



Nitrogen-doped CoP as robust electrocatalyst for high-efficiency pH-universal hydrogen evolution reaction

Yana Men¹, Peng Li¹, Fulin Yang, Gongzhen Cheng, Shengli Chen*, Wei Luo*

College of Chemistry and Molecular Sciences, Wuhan University, Wuhan, Hubei, 430072, PR China

ARTICLE INFO

Keywords:

Transition metal phosphide
Nitrogen-doping
Hydrogen evolution reaction
pH-universal
DFT

ABSTRACT

Although significant achievements have been made in the development of efficient transition metal phosphide (TMP) based electrocatalysts for hydrogen evolution reaction (HER) under acidic and alkaline media, TMP-based electrocatalysts with remarkable HER performances under neutral media has been rarely reported. Herein, we report the synthesis of nitrogen doped CoP nanoflower grown on conductive carbon cloth (N-CoP/CC) that possesses excellent HER performance, with an overpotential of 74 mV to achieve the current density of 10 mA cm⁻² in 1.0 M PBS (phosphate buffer solution, pH = 7), outperforming almost all the documented non-noble TMP-based electrocatalysts. In addition, the N-CoP/CC also displays Pt-like performance in 1.0 M KOH and 0.5 M H₂SO₄, with overpotentials of 39 and 25 mV to achieve the current density of 10 mA cm⁻², respectively. Density functional theory (DFT) calculations and experimental results reveal that doping with N can efficiently affect the electronic states of Co *d*-orbital and optimize the free energy of hydrogen adsorption (ΔG_{H}) to the optimal value, resulting in enhanced HER performance.

1. Introduction

Hydrogen is regarded as an ideal alternative to traditional fossil fuels owing to its high gravimetric energy density and environmental benignity [1–3]. Currently, electrochemical water splitting through cathodic hydrogen evolution reaction (HER) has been extensively investigated as efficient way for large-scale hydrogen production with high purity [4–6]. To date, although Pt-based materials are regarded as the state-of-the-art pH-universal electrocatalysts toward HER, their large-scale application are severely limited by the scarcity and high-cost [7–10]. Consequently, intensive efforts have been devoted to developing efficient noble metal free electrocatalysts toward HER under acidic media for the application of proton exchange membrane-based electrolyzers and alkaline media for alkaline electrolyzers, respectively [11–14]. Nevertheless, electrocatalysts with remarkable catalytic performances for HER under neutral media are rare, probably due to the hydrogen and oxygen are both generated from water molecular rather than H⁺ and OH⁻. Indeed, in industrial manufacture, water electrolysis under neutral-pH electrolytes without using the formidable strong acids/bases possesses the advantages of safety, and corrosion-free conditions [15]. Therefore, developing high-efficiency noble metal free electrocatalysts for HER under a wide pH values, especially in neutral media is highly desirable, but remains a great challenge.

Recently, transition metal phosphides (TMPs) have attracted great attentions due to their hydrogenase-like catalytic mechanism and expected durability within a wide pH values [16–23]. It is known that TMPs usually possess strong hydrogen bonding ability, leading to the unsatisfied HER performance [24]. Therefore, heteroatom doping has been widely considered as an efficient approach to turn their electronic structures, optimize the Gibbs free energy of hydrogen adsorption (ΔG_{H}) and further boost their HER performances. For example, Sun and coworkers reported Mn-doped CoP nanosheets array with much enhanced HER activity due to the more thermos-neutral hydrogen adsorption free energy than CoP [25]; Wang and coworkers reported hollow Mo-doped CoP nanoarrays with significantly improved HER activity under alkaline media [26]; Lu and coworkers reported Fe-doped CoP electrocatalyst for efficient overall water splitting under alkaline media [27]; Lee and coworkers reported S-doped CoP nanoparticles for superior alkaline overall water splitting due to the improved charge-transfer ability after S doping [28]. Despite great efforts have been made to develop efficient TMP-based electrocatalysts for HER under acidic or alkaline media, only a few TMPs were observed to show moderate HER performance under neutral media [29].

It is generally accepted that doping of nitrogen in catalysts can improve the catalytic performances due to the enhancement of electron-donor properties and conductivities. In this regards, taking the

* Corresponding authors.

E-mail addresses: slchen@whu.edu.cn (S. Chen), wluo@whu.edu.cn (W. Luo).

¹ Both authors contributed equally to this work.

advantage of modified electronic structures, boosted active sites, as well as regulated reaction dynamics, a number of nitrogen-doped carbon materials [30], nitrogen-doped transition metal sulfides [31], and transition metal oxides [32] with much enhanced electrocatalytic performances have been reported. Herein, inspired by the previous works, we reported the synthesis of nitrogen-doped CoP nanoflowers supported on the conductive carbon cloth (N-CoP/CC) and their superior catalytic performances toward HER in a wide pH values, with overpotentials of 74, 39 and 25 mV to achieve the current density of 10 mA cm⁻² in 1.0 M PBS (phosphate buffer solution, pH = 7), 1.0 M KOH and 0.5 M H₂SO₄, respectively. Density functional theory (DFT) calculations and experimental results indicate that doping with nitrogen can affect the electronic states of Co *d*-orbital and optimize the free energy of hydrogen adsorption (ΔG_{*H}) to the optimal value, which can effectively facilitating hydrogen adsorption and desorption, leading to the enhancement of HER activity.

2. Results and discussion

The N-doped CoP nanoflower grown on carbon cloth (N-CoP/CC) was obtained by deposition of nanoflower-like Co(OH)F via a hydrothermal method, followed by annealing treatment with sodium hypophosphite and ammonium bicarbonate, as schematically illustrated in Fig. 1a. Fig. S1 shows the powder X-ray diffraction (XRD) patterns of Co(OH)F, where a series of obvious peaks located at 20.8°, 32.3°, 33.5°, 34.8°, 35.6°, 38.7°, 39.9° and 51.9° can be observed, which are corresponding to the (110), (310), (201), (400), (111), (211), (410) and (221) planes of Co(OH)F (PDF#50-0827), respectively. As shown in the scanning electron microscope (SEM) images, Co(OH)F with a nanoflower morphology formed by nanoneedle-array is observed (Fig. S2). After phosphorization and nitridation, the morphology of N-doped CoP is maintained well as shown in Fig. 1(b–d). In the XRD patterns of the N-CoP/CC (Fig. S3), well-matched diffraction peaks located at 31.6°, 36.3°, 46.2°, 48.1°, 52.3° and 56.8° can be observed, which belong to the (011), (111), (112), (211), (103) and (301) planes of CoP (PDF#29-0497) respectively, suggesting the successful formation of CoP. After annealing at 450 °C in the Ar(95%)/H₂(5%), the crystallinity of N-CoP is enhanced as shown in the Fig. S4. The transmission electron microscopy (TEM) image further confirms the nanoneedle-array of N-CoP (Fig. 1e). In addition, the high-resolution TEM (HRTEM) image confirms the crystallinity of N-CoP (Fig. 1f), showing two kinds of obvious lattice fringes with interspaces of about 0.189 and 0.279 nm, corresponding to the (211) and (002) planes of CoP, respectively. The dihedral angle between the two planes is measured to be 70.2°. High-angle annular dark-field scanning transmission electron microscopy (HAADF-STEM), energy-dispersive X-ray spectroscopy (EDX) and corresponding elemental mapping images indicate N, Co, P are uniformly distributed over the entire nanoneedle-array. (Fig. 1g, S5). For comparison, CoP/CC nanoflower was also prepared by the same method without ammonium bicarbonate. The XRD and SEM are shown in Figs.

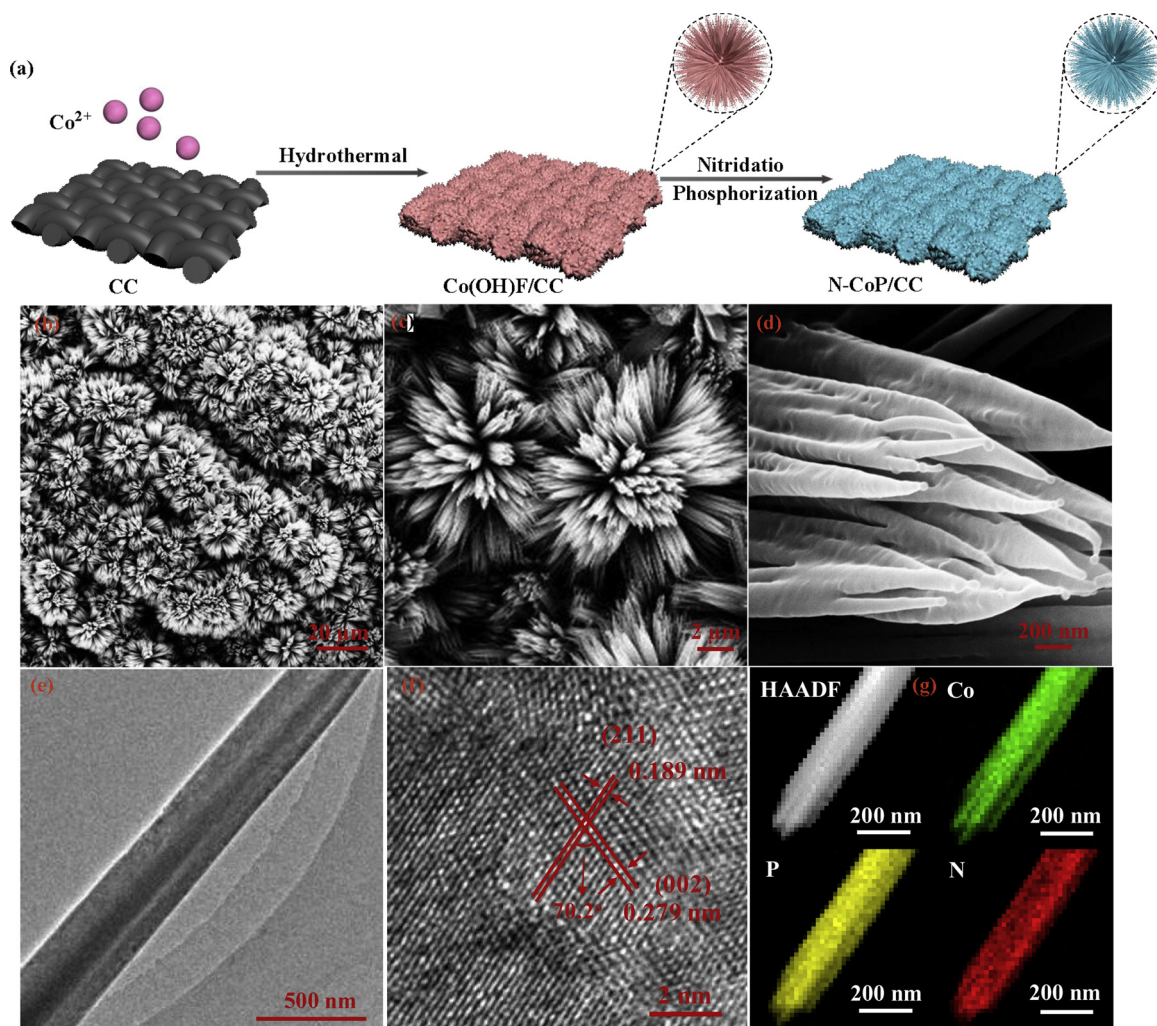


Fig. 1. (a) Schematic of the synthesis process of N-CoP/CC. (b–d) SEM images of N-CoP/CC. (e–f) TEM images of N-CoP/CC. (g) TEM-EDX elemental mapping images of N-CoP/CC.

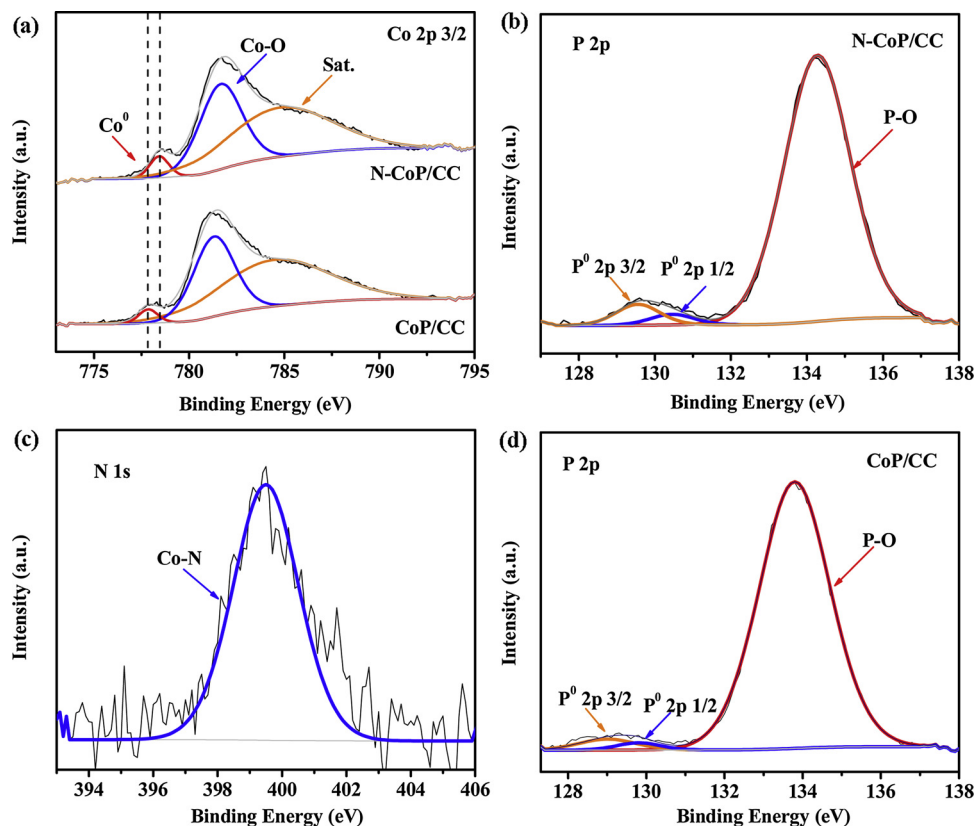


Fig. 2. (a) The XPS of Co 2p spectra for N-CoP/CC and CoP/CC. (b) The XPS of P 2p spectra for N-CoP/CC. (c) The XPS of N 1s spectra for N-CoP/CC. (d) The XPS of P 2p spectra for CoP/CC.

S3 and S6, respectively.

The chemical states of N-CoP/CC and CoP/CC were also studied by X-ray photoelectron spectroscopy (XPS). As shown in Fig. 2a, the Co 2p 3/2 spectrum of N-CoP/CC can be deconvoluted into 778.4, 781.6 and 784.7 eV, corresponding to the Co⁰, Co-O and satellite peaks, respectively. [33,34] Meanwhile, as shown in P 2p spectrum of N-CoP/CC (Fig. 2b), the peaks located at 130.5 and 129.6 eV can be assigned to the P⁰ 2p 1/2 and P⁰ 2p 3/2, respectively. The peak located at 134.3 eV is P-O. [35,36] The appearance of oxide species might be due to surface oxidation on account of exposure to air [37]. In the N 1s spectrum of N-CoP/CC (Fig. 2c), the peak located at 399.4 eV can be assigned to the Co-N, suggesting the doping of the N into CoP [38,39]. It can be seen clearly that the peak of Co⁰ in N-CoP/CC has a positive shift of about 0.6 eV compared with that of CoP/CC (777.8 eV) (Fig. 2a). Furthermore, the peaks of P⁰ 2p 1/2 and P⁰ 2p 3/2 in N-CoP/CC exhibit a positive shift of about 0.7 eV and 0.6 eV compared with those of CoP/CC, respectively. These results demonstrate the electron transfer between N and Co, P, resulting in optimized surface electronic structure of Co and P after nitrogen doping, which is beneficial for the enhanced HER activity (vide infra).

The electrocatalytic activity of all the samples toward HER test were first conducted in a three-electrode system in 1.0 M PBS. As shown in Fig. 3a, N-CoP/CC exhibits an overpotential of 74 mV at the current density of 10 mA cm⁻², which is slightly higher than that of commercial Pt/CC (32 mV), but far lower than that of CoP/CC (136 mV) and among the top of most reported TMP-based electrocatalysts in neutral media (Table S1). In order to further explore HER mechanism for the enhanced activity of N-CoP/CC, we also measured the Tafel slopes of all samples. As shown in Fig. 3b, N-CoP/CC exhibits Tafel slope of 69 mV dec⁻¹, which is close to that of Pt (61 mV dec⁻¹) and much lower than that of CoP (117 mV dec⁻¹). This result indicates N-CoP/CC might follow the Volmer-Heyrovsky mechanism ($\text{H}_2\text{O} + \text{e}^- = \text{H}_{\text{ad}} + \text{OH}^-$ and $\text{H}_2\text{O} + \text{H}_{\text{ad}} + \text{e}^- \rightarrow \text{H}_2 \uparrow + \text{OH}^-$) for the HER in the neutral media

[40]. In addition, the electrochemical impedance spectroscopy (EIS) measurements for N-CoP/CC and CoP/CC were also performed. In the Nyquist plots (Fig. 3c and Fig. S7), N-CoP/CC exhibits a much smaller semicircle than CoP/CC in the high frequency region, indicating smaller charge-transfer resistance and higher electrical conductivity of N-CoP/CC. This enhancement in electrical conductivity for N-CoP/CC is beneficial for the fast charge transfer and electron transport during the HER process, resulting in boosting HER performance. To further investigate the intrinsic activity of catalysts, the electrochemical surface areas (ECSA) of the as-synthesized catalysts were also studied by testing the double layer capacitance (C_{dl}) at varied scan rates from 10 mV s⁻¹ to 50 mV s⁻¹. As shown in Fig. S8, the (C_{dl}) value for N-CoP/CC is calculated to be 120.1 mF cm⁻², which is higher than that of CoP/CC (88.9 mF cm⁻²), suggesting the higher ECSA of N-CoP/CC. In addition, the electrochemical stability test for N-CoP/CC was also conducted. As shown in Fig. 3d, even after 1000 cycles of CV test, there is negligible decline compared with the first cycle. The chronopotentiometry test (the embedded figure in Fig. 3d) confirms that the durability of N-CoP/CC is maintained well even over 30 h. Furthermore, characterizations of N-CoP/CC after HER stability test indicate the well-matched CoP phase from XRD (Fig. S9a), and well-maintained morphology from SEM (Fig. S9b and Fig. S9c). In addition, in the XPS spectra of the Co 2p (Fig. S10a), the metal Co⁰ disappeared after the durability test, possibly because of the formation of cobalt hydroxide on the electrode surface. [41] The peaks of Co 2p 3/2 and Co 2p 1/2 at 780.3 eV and 796.1 eV are belong to the Co-O. The satellite peaks are observed at 780.3 eV and 796.1 eV. The formation of the Co-O was possibly due to the surface oxidation during the stability test in neutral, which agrees well with the previous reports [42]. Meanwhile, the XPS spectra of the P 2p (Fig. S10b) and N 1s (Fig. S10c) are almost kept unchanged. In addition, we also conducted the chronopotentiometric reaction to obtain the Faradaic efficiency. As shown in Fig. S11, the experimentally measured gas values are consistent with the theoretically calculated gas values,

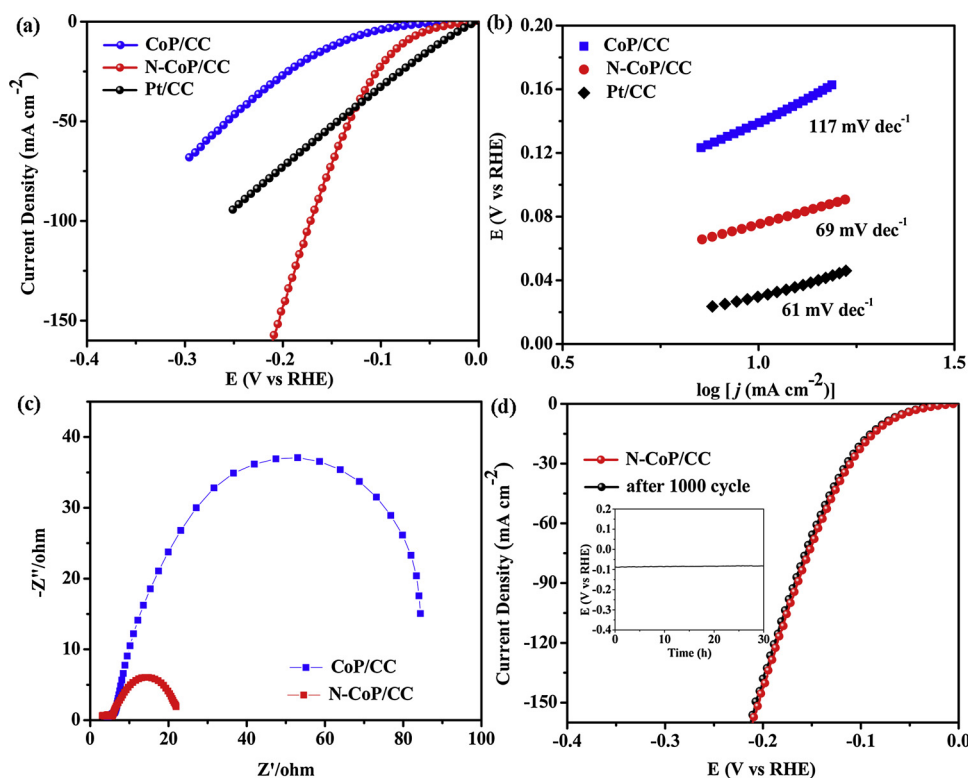


Fig. 3. (a) HER polarization curves of Pt/C, CoP/CC, and N-CoP/CC in 1.0 M PBS. (b) The corresponding Tafel of the samples in 1.0 M PBS. (c) Nyquist plots of CoP/CC, and N-CoP/CC from 10 kHz to 0.01 Hz. (d) Polarization curves of N-CoP/CC at the first cycle and after 1000 cycles and the embedded picture is the chronopotentiometric curve with a constant current density of 10 mA cm⁻² for 30 h in 1.0 M PBS.

suggesting almost 100% Faradaic efficiency.

The HER performances of N-CoP/CC, CoP/CC, and Pt/CC were investigated in 1.0 M KOH as well. As shown in the Fig. 4a, N-CoP/CC needs only an overpotential of 39 mV to reach the current density of 10 mA cm⁻², which is very closed to that of commercial Pt/CC (29 mV)

and far lower than that of CoP/CC (87 mV). It is worth noting that this value is among the best of recently reported non-noble metal based catalysts in alkaline media (Table S2). The Tafel slope of N-CoP/CC is measured to be 58 mV dec⁻¹ (Fig. 4b), which is close to that of Pt/CC (40 mV dec⁻¹) and lower than that of CoP (72 mV dec⁻¹), suggesting

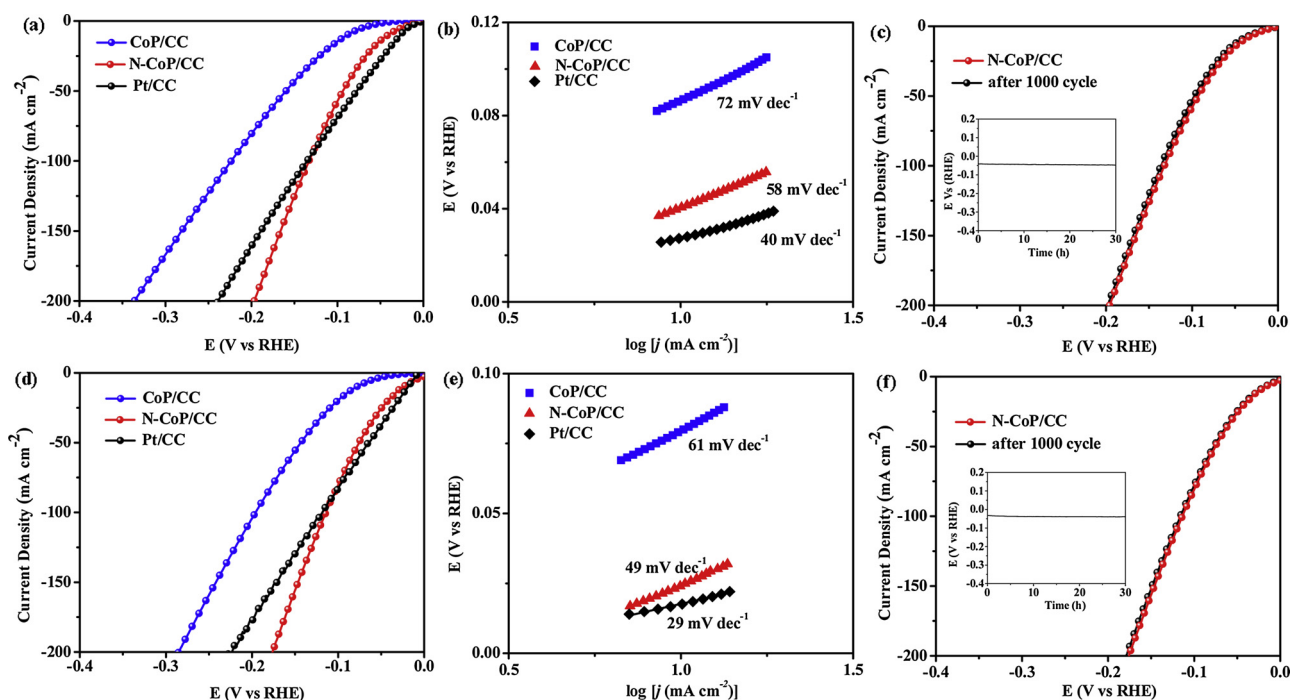


Fig. 4. (a) HER polarization curves of Pt/C, CoP/CC, and N-CoP/CC in 1.0 M KOH. (b) The corresponding Tafel of the samples in 1.0 M KOH. (c) Polarization curves of N-CoP/CC at the first cycle and after 1000 cycles and the embedded picture is the chronopotentiometric curve with a constant current density of 10 mA cm⁻² for 30 h in 1 M KOH. (d) HER polarization curves of Pt/C, CoP/CC, and N-CoP/CC in 0.5 M H₂SO₄. (e) The corresponding Tafel of the samples in 0.5 M H₂SO₄. (f) Polarization curves of N-CoP/CC at the first cycle and after 1000 cycles and the embedded picture is the chronopotentiometric curve with a constant current density of 10 mA cm⁻² for 30 h in 0.5 M H₂SO₄.

the Volmer–Heyrovsky mechanism for the HER in 1.0 M KOH [43]. Meanwhile, in the Nyquist plot (Fig. S12), comparing with that of CoP/CC, the much smaller semicircle of N-CoP/CC indicates N-CoP/CC possessing smaller charge-transfer resistance and higher electrical conductivity. Meanwhile, as shown in Fig. S13, the (C_{dl}) value of N-CoP/CC (192.9 mF cm^{-2}) is higher than that of CoP/CC (140.6 mF cm^{-2}). Furthermore, as shown in Fig. 4c, even after 1000 cycles test for HER, there is negligible degradation comparing with the first cycle. Moreover, the durability of N-CoP/CC could be maintained well even over 30 h as shown in Fig. 4c. After the durability test, no obvious change in the XRD and morphology of N-CoP/CC (Fig. S14) could be observed, indicating its superior stability in 1.0 M KOH. In addition, in the XPS spectra of Co 2p (Fig. S15a), the disappearance of metal Co⁰ after the durability test is observed, which is similar to that in neutral. The formation of the Co-O might be due to the surface oxidation during the stability test in alkaline. [44] There is almost no obvious change in the XPS spectra of the P 2p (Fig. S15b) and N 1s (Fig. S15c). In addition, well-matched point plot in Fig. S16 implies that almost 100% Faradaic efficiency for HER in 1.0 M KOH.

The superb HER performance of N-CoP/CC was also studied in 0.5 M H₂SO₄. As shown in the Fig. 4d, the commercial Pt/CC has the lowest overpotential (19 mV) in the current density of 10 mA cm^{-2} and smallest Tafel slope (29 mV dec^{-1}) (Fig. 4e). In order to achieve the current density of 10 mA cm^{-2} , only an overpotential of 25 mV for the N-CoP/CC is needed, which is much lower than that of CoP/CC (79 mV) and most recently reported non-noble metal based electrocatalysts in acidic solution as indicated in Table S3. Comparing with CoP/CC (61 mV dec^{-1}), the smaller Tafel slope of N-CoP/CC (49 mV dec^{-1}) indicated the faster kinetics following a Volmer–Heyrovsky mechanism for the HER in acidic media. The Nyquist plot in Fig. S17 demonstrates that N-CoP/CC possesses the smaller charge-transfer resistance and higher electrical conductivity comparing with that of CoP/CC. Meanwhile, comparing with CoP/CC (124.8 mF cm^{-2}), N-CoP/CC exhibits much higher (C_{dl}) value (177.8 mF cm^{-2}) (Fig. S18). Furthermore, as shown in Fig. 4f, continuous CV scanning and chronopotentiometric curves indicate the superb long-term durability of N-CoP/CC toward HER in acidic media. Meanwhile, the unchanged XRD and well maintained morphology of N-CoP/CC (Fig. S19) further demonstrate the considerable stability of N-CoP/CC. In addition, after the durability test, no obvious change in the XPS spectra of Co 2p, P 2p, and N 1s (Fig. S20) are observed. Meanwhile, it can be seen unambiguously that the HER reaction catalyzed by N-CoP/CC exhibit almost 100% Faradaic efficiency in the 0.5 M H₂SO₄ as shown in Fig. S21.

To get further insight into the remarkable HER performance of N-CoP, density functional theory (DFT) calculations were carried out (See the Supporting Information for computation details). It is well known that the free energy of hydrogen adsorption (ΔG_{*H}) is an effective descriptor for evaluating the HER activity of electrocatalysts. Catalysts with ΔG_{*H} close to zero are considered as promising candidates for HER [45–47]. To this end, we systematically explored the tuning effects on the intrinsic HER active sites of pristine CoP by N doping for facilitating hydrogen adsorption and desorption (Fig. S22–S26). As shown in Fig. 5a, the pristine CoP (210) exhibits a ΔG_{*H} value of -1.003 eV , indicating the relatively strong *H adsorption. After N doping, the ΔG_{*H} of N-CoP (210) increased to -0.314 eV , which is much more thermoneutral than the pristine CoP (210), supporting its higher HER performance. In our DFT calculations, the most stable adsorption site of *H is the Co-Co bridge site on both pristine CoP and N-CoP, which is in consistent with previous reports. [48,49] Due to the major contribution of H bonding from Co *d*-orbital electrons, changes in the electronic states of Co *d*-orbital will have a crucial effect on the binding strength of *H and corresponding HER performance. Therefore, we performed Mulliken population analysis on pristine CoP and N-CoP, to determine the electron transfer quantitatively. As shown in Fig. 5b, by comparing the charge population of N-CoP (210) with that of pristine CoP (210), we found that both two Co atoms of the Co-Co bridge site (highlighted

by the yellow stars) transfer about 0.2 more electrons to the doped N atom than pristine P atom, due to the relatively stronger electronegativity of N than P. Thus, the decreased electron density of Co *d*-orbital in N-CoP induced by the substitution of N for P leads to the weaker binding strength of H. In addition, we have calculated the electron density difference of the Co-H bonding region (marked by the black dashed line in Fig. 5c) between N-CoP (210) with an adsorbed H and pristine CoP (210) with an adsorbed H (seeing Fig. S27 for details). It is clear to see that the electron density of Co-H bonding region is decreased after the N doping, resulting in the reduced bonding interaction between Co and H, which is in consistent with the results of H adsorption free energy calculations and Mulliken population analysis. As expected, this trend has also been verified by choosing CoP (111) and N-CoP (111) to study the changes in hydrogen adsorption free energy before and after the N doping (Fig. 5a and Fig. S25). In addition, we also conducted the HER tests of CoP/CC with various N doping contents (Fig. S28) by altering the amount of ammonium bicarbonate to study the influences of different N doping amount toward the HER performance. The different amount of N doping were analyzed by XPS characterization (Fig. S29, Table S4). [50] The LSV curves (Fig. S30) and DFT calculations (Fig. S31) suggest that the optimal N-doping content is 7.8%, in which the obtained N-CoP/CC showed the highest HER performance in all pH values due to the optimized H adsorption.

3. Conclusion

In summary, we have successfully synthesized N-CoP nanoflower grown on CC for boosting pH-universal HER performances. Benefiting from the highly opened morphology with high exposure of active sites, as well as the enhanced electrical conductivity and synergistic electronic effect after nitrogen doping, the resultant N-CoP/CC displays outstanding HER activity and stability. Particularly, it shows Pt-like activity with overpotentials of 74, 39 and 25 mV to reach the current density of 10 mA cm^{-2} with good stability in 1.0 M PBS, 1.0 M KOH and 0.5 M H₂SO₄, respectively, outperforming most of the reported TMP-based electrocatalysts. DFT calculations indicate that doping with N could optimize the free energy of adsorbed H (ΔG_{*H}) of CoP to optimal value, which can benefit the HER process. This strategy herein highlights the N-doping in favor of modification of highly efficient TMP-based electrocatalysts, and can be extended to the design of other electrocatalysts with high efficiency for more applications.

4. Experimental section

4.1. Preparation of Co(OH)F/CC nanoflower

The carbon cloth (CC) obtained from Ce Tech Co. Ltd. was treated with acetone, water and ethanol by sonication treatment for 15 min, respectively. Then, 1.2 mmol of Co(NO₃)₂·6H₂O, 4.8 mmol of NH₄F and 6 mmol of CO(NH₂)₂ were dissolved in 15 mL of deionized water, which were stirred for 30 min. After this step, the obtained mixed solution and carbon cloth were transferred into a 20 mL Teflon-lined stainless steel autoclave and kept at 120 °C for 6 h. After the reaction, the obtained Co (OH)F/CC was washed by water and ethanol and dried at 60 °C in vacuum drying chamber overnight.

4.2. Preparation of N-doped CoP/CC and CoP/CC nanoflower

To prepare the N-doped CoP/CC nanoflower, the obtained Co(OH)F/CC was placed at the lower reaches of the quartz tube, 300 mg of NaH₂PO₂ was put at the upper reaches of the quartz tube, and 120 mg ammonium bicarbonate was put at the 2/3 places near the upper reaches. The quartz tube were annealing at 300 °C for 2 h with a heating rate of $2^\circ \text{C min}^{-1}$ under Ar atmosphere. The CoP/CC nanoflower was obtained by the same method except without adding the ammonium bicarbonate.

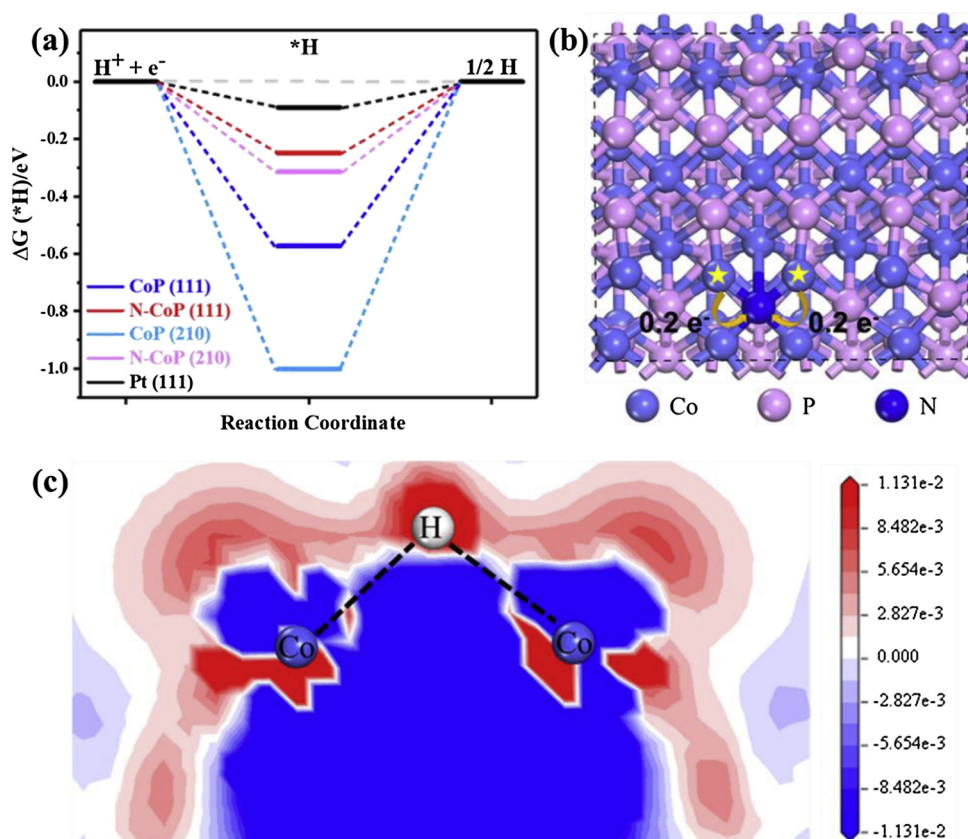


Fig. 5. (a) The free energy diagram for HER on Pt (111), CoP (111) and CoP (210) surfaces with and without N-doping. The ΔG_{*H} of Pt (111) equates -0.09 eV according to the previous DFT work. (b) The schematic of the electron transfer from Co to N after the substitution of N for P for CoP (210) surface. (c) The electron density difference of Co-H bonding region between the H adsorbed N-CoP (210) surface and the H adsorbed pristine CoP (210) surface.

4.3. Electrochemical measurements

We used a CHI-760E electrochemistry workstation to perform electrochemical tests at room temperature and under a hydrogen saturated atmosphere. For all electrochemical tests, three-electrode system was applied, in which our electrocatalyst as the working electrode, the carbon rod with a diameter of 5 mm as the counter electrode and the saturated calomel electrode (SCE) in acid and neutral (Hg/HgO in base) as the reference electrode. All the measured potentials were referred to reversible hydrogen electrode (RHE). The conversion formulas are E (vs RHE) = E (vs SCE) + $0.059 \cdot \text{pH} + 0.242$ and E (vs RHE) = E (vs Hg/HgO) + $0.059 \cdot \text{pH} + 0.098$ for saturated calomel electrode (SCE) and Hg/HgO electrode, respectively. The loading amount of the N-CoP catalyst on carbon cloth (CC) was about 5 mg cm^{-2} . Before the electrochemical tests, all of the electrocatalysts were firstly activated by continuous cyclic voltammetry (CV) for several cycles. Then, we carried out the linear sweep voltammetry (LSV) tests with a scan rate of 2 mV s^{-1} . The stability tests of the N-CoP/CC were performed by cycling it for 1000 times at a scan rate of 100 mV s^{-1} in the potential range from 0.02 V to -0.22 V (V vs RHE) in the acid and alkaline electrolyte and from 0.02 V to -0.25 V in neutral media, respectively. Following, the chronopotentiometry tests were performed at the constant current density of 10 mA cm^{-2} . What's more, we have performed the electrochemical impedance spectroscopies (EIS) measurements at the overpotential of 80 mV , 40 mV and 30 mV in 1.0 M PBS , 1.0 M KOH and $0.5 \text{ M H}_2\text{SO}_4$, respectively. Finally, the electrochemical double-layer capacitance (C_{dl}) measurements have been carried out by using cyclic voltammetry curves with different scanning rates of 10 , 20 , 30 , 40 and 50 mV s^{-1} . All the LSV data were corrected by IR compensation.

4.4. Material characterization

The X-ray diffraction (XRD) patterns were carried out on a Bruker D8-Advance X-ray diffractometer with a Cu K α radiation source

($\lambda = 0.154178 \text{ nm}$). The X-ray photoelectron spectroscopy (XPS) patterns were performed at a Thermo Fischer ESCALAB 250Xi Spectrophotometer with the excitation source of monochromatic aluminum. Our scanning electron microscope (SEM) images were obtained from the Zeiss Sigma Scanning Electron Microscope device. A Tecnai G20 U-Twin Transmission Electron Microscope equipped with an energy dispersive X-ray detector was used to get the transmission electron microscope (TEM) images and energy-dispersive X-ray spectroscopy (EDS) elemental mapping images.

Acknowledgements

This work was financially supported by the National Natural Science Foundation of China (21571145, 21633008), and Large-scale Instrument and Equipment Sharing Foundation of Wuhan University. The DFT calculations in this paper have been done on the supercomputing system in the Supercomputing Center of Wuhan University.

Appendix A. Supplementary data

Supplementary material related to this article can be found, in the online version, at doi:<https://doi.org/10.1016/j.apcatb.2019.04.038>.

References

- [1] H. Lv, X. Chen, D. Cu, Y. Hu, H. Zheng, S.L. Suib, B. Liu, Appl. Catal. B Environ. 238 (2018) 525–532.
- [2] Y. Li, K. Yin, L. Wang, X. Lu, Y. Zhang, Y. Liu, D. Yan, Y. Song, S. Luo, Appl. Catal. B Environ. 239 (2018) 537–544.
- [3] S.D. Ebbesen, S.H. Jensen, A. Hauch, M.B. Mogensen, Chem. Rev. 114 (2014) 10697–10734.
- [4] Y. Yan, B. Xia, Z. Xu, X. Wang, ACS Catal. 4 (2014) 1693–1705.
- [5] S. Jing, L. Zhang, L. Luo, J. Lu, S. Yin, P. Shen, P. Tsiakaras, Appl. Catal. B Environ. 224 (2018) 533–540.
- [6] H. Man, C. Tsang, M. Li, J. Mo, B. Huang, L.Y.S. Lee, Y. Leung, K. Womh, S.C.E. Tsang, Appl. Catal. B Environ. 242 (2019) 186–193.
- [7] P. Chen, T. Zhou, M. Zhang, Y. Tong, C. Zhong, N. Zhang, L. Zhang, C. Wu, Y. Xie,

- Adv. Mater. 29 (2017) 1701584.
- [8] Y. Zheng, Y. Jiao, M. Jaroniec, S.Z. Qiao, *Angew. Chem. Int. Ed.* 54 (2015) 52–65.
- [9] Z. Pu, S. Wei, Z. Chen, S.C. Mu, *Appl. Catal. B Environ.* 196 (2016) 193–198.
- [10] Q. Mo, W. Zhang, L. He, X. Yu, Q.S. Gao, *Appl. Catal. B Environ.* 244 (2019) 620–627.
- [11] M.R. Gao, J.X. Liang, Y.R. Zheng, Y.F. Xu, J. Jiang, Q. Gao, J. Li, S.H. Yu, *Nat. Commun.* 6 (2015) 5982.
- [12] Y. Tang, H. Zhu, L. Dong, A. Zhang, S. Li, J. Liu, Y.Q. Lan, *Appl. Catal. B Environ.* 245 (2019) 528–535.
- [13] F. Wang, Y. Li, T.A. Shifa, K. Liu, F. Wang, Z. Wang, Q.J. Wang, J. He, *Angew. Chem. Int. Ed.* 24 (2016) 6919–6924.
- [14] Y. Tan, H. Wang, P. Liu, Y. Shen, C. Cheng, A. Hirata, M. Chen, *Energy Environ. Sci.* 9 (2016) 478–483.
- [15] K.A. Vincent, A. Parkin, F.A. Armstrong, *Chem. Rev.* 107 (2007) 4366–4413.
- [16] Y. Shi, B. Zhang, *Chem. Soc. Rev.* 45 (2016) 1529–1541.
- [17] Y. Huang, X. Song, J. Deeng, C. Zha, W. Huang, Y. Wu, Y. Li, *Appl. Catal. B Environ.* 245 (2019) 656–661.
- [18] C. Du, L. Yang, F. Yang, G.Z. Cheng, S.L. Chen, W. Luo, *ACS Catal.* 7 (2017) 4131–4137.
- [19] T. Liu, D. Liu, F. Qu, D. Wang, L. Zhang, R. Ge, L. Chen, *Adv. Energy Mater.* 7 (2017) 1700020.
- [20] J. Tian, Q. Liu, A.M. Asiri, X. Sun, *J. Am. Chem. Soc.* 136 (2014) 7587–7590.
- [21] T. Liu, K. Wang, G. Du, A.M. Asiri, X. Sun, *J. Mater. Chem. A* 4 (2016) 13053–13057.
- [22] Y. Ji, L. Yang, X. Ren, G. Cui, X. Xiong, X. Sun, *ACS Sustain. Chem. Eng.* 6 (2018) 11186–11189.
- [23] Z. Wang, X. Ren, Y. Luo, L. Wang, G. Cui, F. Xie, X. Sun, *Nanoscale* 10 (2018) 12302–12307.
- [24] F.L. Yang, Y.T. Chen, G.Z. Cheng, S.L. Chen, W. Luo, *ACS Catal.* 7 (2017) 3824–3831.
- [25] T. Liu, X. Ma, D. Liu, S. Hao, G. Du, Y. Ma, A.M. Asiri, X.P. Sun, L. Chen, *ACS Catal.* 7 (2017) 98–102.
- [26] C. Guan, W. Xiao, H. Wu, X. Liu, W. Zang, H. Zhang, S.J. Pennycook, J. Wang, *Nano Energy* 48 (2018) 73–80.
- [27] L.M. Cao, Y.W. Hu, S.F. Tang, A. Iljin, J.W. Wang, Z.M. Zhang, T.B. Lu, *Adv. Sci.* 5 (2018) 1800949.
- [28] M.A.R. Anjum, M.S. Okyay, M. Kim, M.H. Lee, N. Park, J.S. Lee, *Nano Energy* 53 (2018) 286–295.
- [29] S.U. Hettiarachchi, B. Prasai, R.L. McCarley, *J. Am. Chem. Soc.* 136 (2014) 7575–7578.
- [30] Z. Chen, Y. Song, J. Cai, X. Zheng, D. Han, Y. Wu, Y.P. Zang, S.W. Niu, Y. Liu, J.F. Zhu, X. Liu, *Angew. Chem. Int. Ed.* 57 (2018) 5076–5080.
- [31] Y. Wu, X. Liu, D. Han, X. Song, L. Shi, Y. Song, J. Kang, J.B. Zhou, Z.Y. Chen, X.S. Zheng, X.H. Xiao, G.M. Wang, *Nat. Commun.* 9 (2018) 1425.
- [32] M.H. Yu, Z.K. Wang, C. Hou, Z.L. Wang, C. Liang, C.L. Zhao, Y.X. Tong, X.H. Lu, S.H. Yang, *Adv. Mater.* 29 (2017) 1602868.
- [33] C. Tang, R. Zhang, W.B. Lu, L.B. He, X. Jiang, A.M. Asiri, X.P. Sun, *Adv. Mater.* 29 (2017) 1602441.
- [34] W. Gao, M. Yan, H.Y. Cheung, Z.M. Xia, X. Zhou, Y.B. Qin, C.Y. Wong, J.C. Ho, C.R. Chang, Y.Q. Qu, *Nano Energy* 38 (2017) 290–296.
- [35] T.P. Moffat, R.M. Latanision, R.R. Ruf, *Electrochim. Acta* 40 (1995) 1723–1734.
- [36] C.J. Powell, *J. Electron. Spectrosc.* 185 (2012) 1–3.
- [37] X. Xiao, L.M. Tao, M. Li, X.W. Lv, D.K. Huang, X.X. Jiang, H.P. Pan, M.K. Wang, Y. Shen, *Chem. Sci.* 9 (2018) 1970–1975.
- [38] T. Zhou, Y. Du, S. Yin, X. Tian, H. Yang, X. Wang, B. Liu, H.M. Zheng, S.Z. Qiao, R. Xu, *Energy Environ. Sci.* 9 (2016) 2563–2570.
- [39] J.M. Ziegelbauer, T.S. Olson, S. Pylypenko, F. Alamgir, C. Jaye, P. Atanassov, S. Mukerjee, *J. Phys. Chem. C* 112 (2008) 8839–8849.
- [40] Y. Shi, B. Zhang, *Chem. Soc. Rev.* 45 (2016) 1529–1541.
- [41] Y. Zhang, L. Gao, E.J. Hensen, J.P. Hofmann, *ACS Energy Lett.* 3 (2018) 1360–1365.
- [42] L. Zhang, P.F. Liu, Y.H. Li, C.W. Wang, M.Y. Zu, H.Q. Fu, X.H. Yang, H.G. Yang, *ACS Catal.* 8 (2018) 5200–5205.
- [43] T. Liu, X. Ma, D.N. Liu, S. Hao, G. Du, Y.J. Ma, A.M. Asiri, X.P. Sun, *ACS Catal.* 7 (2016) 98–102.
- [44] Y. Zhang, L. Gao, E.J. Hensen, J.P. Hofmann, *ACS Energy Lett.* 3 (2018) 1360–1365.
- [45] Y.P. Liu, G.T. Yu, G.D. Li, Y.H. Sun, T. Asefa, W. Chen, X.X. Zou, *Angew. Chem. Int. Ed.* 127 (2015) 10902–10907.
- [46] J.S. Li, Y. Wang, C.H. Liu, S.L. Li, Y.G. Wang, L.Z. Dong, Z.H. Dai, Y.F. Li, Y.Q. Lan, *Nat. Commun.* 7 (2016) 11204.
- [47] H.B. Zhang, Z.J. Ma, J.J. Duan, H.M. Liu, G.G. Liu, T. Wang, K. Chang, M. Li, L. Shi, X.G. Meng, K.C. Wu, J.H. Ye, *ACS Nano* 10 (2016) 684–694.
- [48] C. Tang, L.F. Gan, R. Zhang, W.B. Lu, X. Jiang, A.M. Asiri, X.P. Sun, J. Wang, L. Chen, *Nano Lett.* 16 (2016) 6617–6621.
- [49] Y. Pan, K. Sun, S.J. Liu, X. Cao, K.L. Wu, W.C. Cheong, Z. Chen, Y. Li, Y. Wang, Y.Q. Liu, D.S. Wang, Q. Peng, C. Chen, Y.D. Li, *J. Am. Chem. Soc.* 140 (2018) 2610–2618.
- [50] Z.L. Wang, X.F. Hao, Z. Jiang, X.P. Sun, D. Xu, J. Wang, X.B. Zhang, *J. Am. Chem. Soc.* 137 (2015) 15070–15073.